CrystEngComm

Stable yellow ZnO mesocrystals with excellent visible light photocatalytic activity

SCHOLARONE™
Manuscripts

[JOURNAL NAME HERE] | www.rsc.org/[JOURNAL]   **Paper**

Stable yellow ZnO mesocrystals with efficient visible light photocatalytic activity

Yin Peng[a], Yu Wang[a], Qing-Guo Chen[a], Qing Zhu[b] and An Wu Xu[b]*

5

Band gap narrowing is of significance and advantage for potential visible light photocatalytic applications. Here we have reported an effective strategy for the large-scale synthesis of yellow ZnO mesocrystals with narrow band-gap (Eg = 3.09 eV) and visible light response using Zn(OH)F precursors. Raman and X-ray photoelectron spectroscopy (XPS) spectra reveal that a large amount of oxygen vacancies exist in the yellow ZnO mesocrystals, and the concentration of oxygen defects decreases with an increase of annealing temperature in air. Oxygen vacancies result in a narrowing band-gap and increase the visible light response of the yellow ZnO. Electron paramagnetic resonance (EPR) spectra confirm that abundant surface defects exist in yellow ZnO, leading to strong photoluminescence emission. The yellow ZnO mesocrystal is found to be efficient for photodecomposition of methyl blue (MB) under visible light irradiation. It is demonstrated that highly ordered porous mesocrystals are favorable for directional transport and high efficient separation of charge carriers. Notably, our yellow ZnO ring sample is very stable for at least one year. Therefore, our present work highlights the feasibility of simultaneously engineering of oxygen vacancies and visible light response for designing novel ZnO-based materials for solar energy conversion.

Introduction

More research interests have focused on the search for cost-effective, sustainable and green energy sources to meet the global energy demands because of increasing environmental contaminations and growing threat of current energy crisis. The use of solar energy for complete removal of organic pollutants on highly effective photocatalysts has long been regarded as the ultimate solution in that semiconductor based photocatalysis takes place at ambient temperature via green chemical process.[1] The increasing demand for low cost and highly efficient materials capable of solar energy generation and conversion is much desired. Metal oxides, as a family of attractive and promising materials, have been widely investigated for photocatalytic applications owing to its relatively high chemical stability, abundance, low-cost and non-toxicity.

A mesocrystal is a quasi-single crystal consisting of individual nanocrystals (size within the mesoscale) as the subunits, these building blocks are vectorially aligned in a common crystallographyic mode and form an entirely new class of porous superstructures with rough surface and elongated electron diffraction pattern similar to that of a single crystal.[2,3] Mesocrystals highlight a general route to design a crystal morphology using anisotroptic subunits, and a new feasibility of constructing multifunctional materials with exciting properties. Now, mesocrystals have attracted interests in materials chemistry, life science and crystallization related fields. In recent years, some semiconductors have been prepared as mesocrystals.[4,5] It is demonstrated that highly ordered porous mesocrystals are favorable for high efficient and directional transport of charge carriers.[6]

Zinc oxide (ZnO), a typical n-type semiconductor with a relatively wide band gap (Eg = 3.24 eV at 300 K) and large excitonic binding energy (60 meV), has attracted a considerable interests owing to its potentials in UV laser devices, piezoelectric nanogenerators, sensors and biomedical labels. Recently, ZnO nanostructures have been used as an alternative to TiO_2 for the UV photocatalytic degradation of organic pollutants due to their non-toxic and high photocatalytic efficiency.[7] It is well known that bulk ZnO has a large band gap and can not be excited by visible light, which greatly restricts the photocatalytic reaction efficiency with visible light or solar light. Because of its no visible light response, it is of significance to extend ZnO nanomaterials to the visible light or solar light response for visible light photocatalytic degradation of contaminants and solar energy conversion devices.

For semiconductor photocatalysts, foreign metal or nonmetal element doping has been widely developed to tune the electronic and band structures of wide band gap metal oxides such as TiO_2 and ZnO. Besides doping with foreign elements, self-doping has also been used to tailor the electronic and band structures of semiconductors,[8-13] such as oxygen-defective TiO_{2-x} and SnO_{2-x}.[8,9] We have recently reported the Sn^{2+} self-doping of SnO_{2-x} nanoparticle enables its efficient absorption in the visible light region and high photocatalytic activity. Justicia et al.[11,13] carried out a series of first-principle calculations to evaluate the effect of oxygen defects on the electronic structures of TiO_{2-x}, and found that the oxygen defects increase the gap states to generate a mini-band below the conduction band. The electrons in these oxygen vacancy states are able to transport and make a contribution to the conduction by harvesting visible light.

Previous studies found that ZnO color turned from white to yellow when ZnO was annealed at high temperature,[14-17] This color change results from the formation of oxygen vacancies in ZnO by calcination. These works inspire us an idea to effectively extend the visible light absorption by introducing oxygen defects

[a]The Key Laboratory of Functional Molecular Solids, Ministry of Education, College of Chemistry and Materials Science, Anhui Normal University, Wuhu 241000, China
[b]Division of Nanomaterials and Chemistry, Hefei National Laboratory for Physical Sciences at Microscale, Department of Chemistry, University of Science and Technology of China, Hefei 230026, P. R China.
Fax: (+86) 551-6360 2346; E-mail: anwuxu@ustc.edu.cn.

in ZnO nanostructures. However, in previous studies, the oxygen vacancies in ZnO are not stable after high temperature calcination treatment, and ZnO gradually changes from yellow to white again when it is cooled down to room temperature. Moreover, the concentration of oxygen vacancies in ZnO samples is usually low, it might not be sufficient to substantially extend ZnO absorption to the visible light regions. Although there have been some studies on the relationship between the oxygen vacancies and photocatalytic performance of ZnO,[18–22] the reports on defect-driven band gap narrowing for ZnO are still limited.[23-26]

Recently, Uekawa's and Jobic's works[27–29] demonstrated that ZnO nanoparticles contained rich oxygen vacancies could be obtained by calcining zinc peroxide nanoparticles at temperature over than 513 K, which inspired us that it might be a simple strategy to incorporate oxygen vacancies into ZnO crystal lattices by annealing some specific precursors. Herein, we prepared yellow ZnO mesocrystals (ZnO-500) with abundant oxygen vacancies by annealing Zn(OH)F precursors at 500 ℃ in air. The influences of annealing temperature on the concentrations of oxygen vacancies in as-made ZnO were systematically explored, as well as the oxygen vacancies driven visible light photocatalytic reactions. The results demonstrate that abundant oxygen vacancies in ZnO samples can efficiently expand the visible light absorption range of ZnO mesocrystals, thus improving visible light photocatalytic activity. Higher oxygen vacancy concentration indeed results in stronger absorption of visible light and band gap narrowing. Moreover, we propose a possible mechanism that is responsible for the narrowing of ZnO band gap and the improvement in visible light photocatalytic activity.

Experimental Section

Synthesis of Zn(OH)F precursor and yellow ZnO mesocrystal.

All chemicals (hexamethylenetetramine (HMT), HF and zinc acetate dihydrate ($Zn(AC)_2 \cdot 2H_2O$)) were of analytical reagent grade and used as received without further purification.

In a typical procedure, 5 mmol of Zn $(AC)_2 \cdot 2H_2O$ was dissolved in 35 mL of deionized water. Then 5 mmol of HMT was added under stirring. The mixture was magnetically stirred for 10 min. And an aqueous solution of 400 μL HF (30 wt %) was gradually added under constant stirring. Then the solution was transferred into a 50 mL Teflon-sealed autoclave and maintained at 160 ℃ for 6 h. After cooled to room temperature, the white Zn(OH)F product was separated from the solution and thoroughly washed several times by deionized water and dried at 60 ℃ in a vacuum oven. The obtained Zn(OH)F precursors were calcined in the air at 500 ℃ and 800 ℃ for 2 h, and the obtained ZnO samples are labeled ZnO-500 and ZnO-800, respectively.

ZnO-ref was obtained by the similar method with ZnO-500 except that HF was not added in the reaction system.

Photocatalytic activity measurements

The photocatalytic activities of the samples were tested by the photocatalytic decomposition of methylene blue (MB) at room temperature with visible light irradiation. Typically, 40 mg of photocatalyst was dispersed in 40 mL of 10 mg/L MB aqueous solution in a reactor of double layer cooled by running water to keep the temperature unchanged. Prior to irradiation, the suspension was magnetically stirred in the dark for 1 h to ensure an adsorption/desorption equilibrium of MB on the surface of the photocatalyst. Then, the suspension was illuminated by the 500 W Xe lamp combined with a UV cutoff filter (λ ⩾ 400 nm)

under stirring. At irradiation time intervals of 30 min, the suspension was withdrawn, and centrifuged to remove the photocatalyst. The degradation of MB was monitored with a UV 1800PC spectrophotometer (Shanghai Mapada Instruments). Additionally, the recycle experiments were performed for five recycles to test the durability. After each cycle, the catalyst was centrifugation and used directly for the next test.

Photoelectrochemical test systems were composed of a CHI 660D electrochemistry potentiostat (Shanghai Chenhua Limited, China), a 300 W xenon lamp with cutoff filters (λ ⩾ 400 nm), and a homemade three-electrode cell with using Pt wire as the counter electrode and Ag/AgCl as reference electrode, and 1 M Na_2SO_4 as electrolyte. ZnO-500, ZnO-800 and ZnO-ref electrodes were prepared by depositing suspensions (the concentration of sample dissolved by absolute ethanol is 10 mg•mL^{-1}) onto Ti foil using the doctor-blade coating method with a glass rod and scotch tape as a frame and spacer, respectively. The electrodes were annealed at 90 ℃ for 24 h. During measurements, the electrodes were pressed against a □-shape of an electrochemical cell with a working area of 4.0 cm^2.

Characterization

The X-ray powder diffraction (XRD) patterns of the products were performed on a Rigaku/Max-3A X-ray diffractometer with Cu Kα radiation (λ = 1.54178 Å), the operation voltage and current was maintained at 40 kV and 200 mA, respectively. The SEM images were taken using a field-emission scanning electron microscope (Hitachi S-4800) operated at an accelerating voltage of 5 kV. Transmission electron microscopic (TEM) images, high-resolution transmission electron microscopic (HRTEM) images and the selected area electron diffraction (SAED) patterns were performed on a JEOL-2010 microscope with an accelerating voltage of 200 kV. UV-vis diffuse-reflectance spectrum was recorded with a UV-2450 spectrophotometer in the wavelength range of 200-800 nm at room temperature. $BaSO_4$ was used as the reflectance standard material. The X-Ray photoelectron spectroscopy (XPS) was performed on a Perkin-Elmer RBD upgraded PHI-5000C ESCA system. Raman spectra were measured with a Perkin–Elmer 400F Raman Spectrometer using a 514.5 nm laser beam. The electron paramagnetic resonance (EPR) spectra were recorded on a JEOL JES-FA200 EPR spectrometer (300 K, 9064 MHz, 0.998 mW, X-band). The g values were determined using a 2,2-diphenyl-1-picrylhydrazyl (DPPH) standard. The photoluminescence emission spectra (PL) were recorded on a FLS920 spectrophotometer equipped with a 150-W xenon lamp as the excitation source at room temperature. Nitrogen adsorption measurements were performed at 77 K using a Micromeritics Tristar II 3020 M analyzer after the samples were degassed at 180 ℃ for 6 h. The Brunauer-Emmett-Teller (BET) surface area was estimated by using adsorption data in a relative pressure range from 0.05 to 0.3.

Results and discussion

The crystal structures of as-prepared Zn(OH)F precursor and the samples obtained after annealing under different temperatures were investigated by X-ray diffraction (XRD). As shown in Figure 1, the diffraction peaks of the precursor could be indexed to orthorhombic phase Zn(OH)F (JCPDS file No.32-1469). The samples obtained from annealing Zn(OH)F at different temperature all display a hexagonal wurtzite structure of ZnO crystals (JCPDS No. 36-1451) with well crystallinity.

[JOURNAL NAME HERE] | www.rsc.org/[JOURNAL]   **Paper**
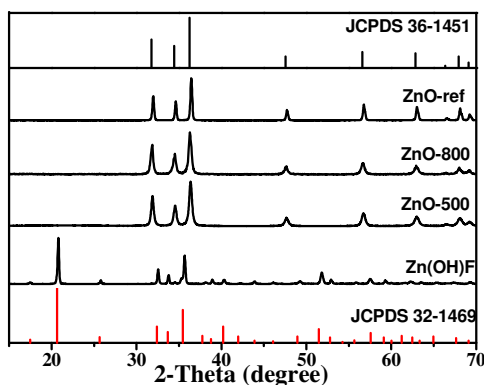
Fig. 1 XRD diffraction pattern of the obtained ZnO with different annealing temperatures and ZnO-ref samples.

The shape and microstructure of the samples were investigated by scanning electron microscopy (SEM). The Zn(OH)F precursor consists almost entirely of uniform hexagonal ring-like structures, as displayed in Figure 2a. These microrings have outer diameters of 5-9 μm, inner diameters of 2.5-4 μm. The hexagonal cross-section of the outer shape and central hole are clearly seen. There is no obvious change of morphology for yellow ZnO denoted ZnO-500 (Figure 2b), which was obtained from calcining Zn(OH)F precursors at 500 °C in air for 2 h. Moreover, some pores can be found on the yellow ZnO rough surface, which were generated by the Zn(OH)F thermal decomposition.

Transmission electron microscopy (TEM) was used to further examine the structures of yellow ZnO-500 mesocrystals. From Figure 2c, it can be found that each ZnO-500 ring has rough surface and many nanopores, in accordance with SEM measurements. High magnified TEM image (Figure 2d) displays that each ring is composed of abundant nanoplates and nanoparticles aligned along the same orientation. The selected area electron diffraction (SAED) pattern (inset of Figure 2d) recorded from the nanoparticles can be readily indexed as a hexagonal ZnO single crystal. From high-resolution TEM (HRTEM, Figure 2e) it is clearly shown that two nanoplates have the same crystallographic orientation along the [010] zone axis, confirming the formation of ZnO mesocrystals, this oriented nanostructure is favorable for directional transfer and efficient separation of electron and hole pairs.[6]

The presence of pores in the ZnO-500 mesocrystals was confirmed by the nitrogen sorption isotherms and Barrett-Joyner-Halenda (BJH) desorption analyses. As shown in Figure 3a, the isotherm is a type IV shape with a type H3 hysteresis loop at high relative pressures according to the IUPAC classification, which indicates that yellow ZnO-500 mesocrystal is mesoporous structures in the pore diameter range of 2-50 nm, which is a typical character of a mesocrystal. This result can be further demonstrated by the corresponding pore size distribution (Figure 3b). It can be clearly seen that yellow ZnO-500 sample is mesoporous structures with the average pore size of 10.7 nm. The formation of mesopores results from the thermal decomposition of Zn(OH)F precursor. The porous structure could increase the photocatalytic activity of yellow ZnO-500 mesocrystals due to its large BET surface area (18 $m^2 \cdot g^{-1}$). It is notable that the yellow color of the obtained ZnO mesocrystals remains unchanged when kept in air for at least one year.
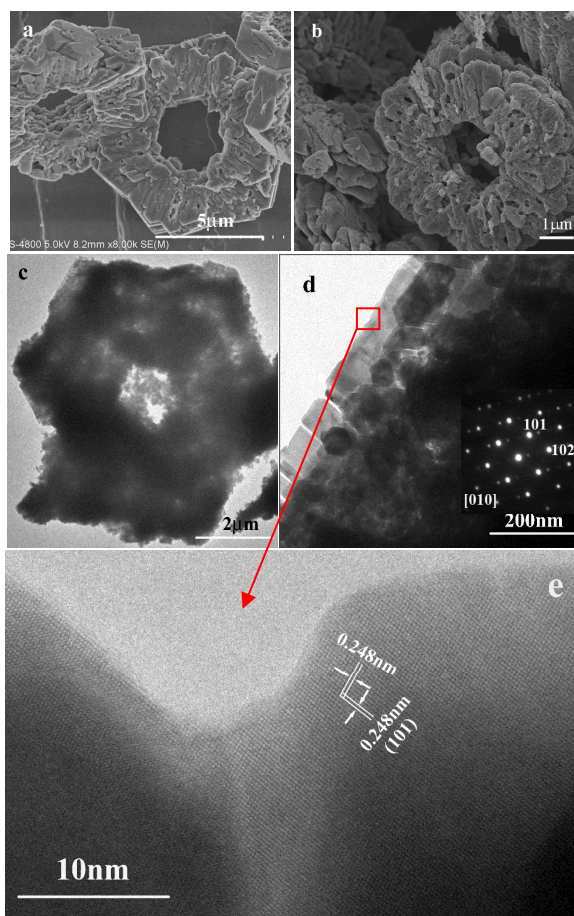
Fig. 2 The SEM images of the Zn(OH)F precursor (a); yellow ZnO-500 mesocrystals obtained by calcining Zn(OH)F at 500 °C in air for 2 h (b); TEM image of a single ZnO-500 ring (c); TEM (d, SAED inset) and HRTEM (e) images taken from a single ZnO-500 mesocrystal.
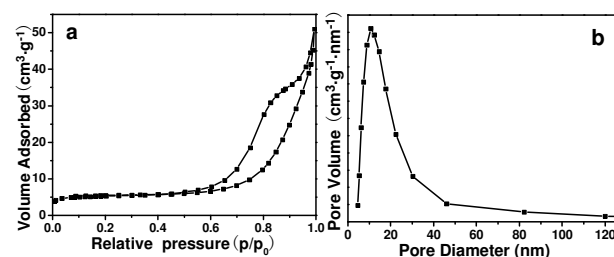
Fig. 3 (a) Nitrogen adsorption-desorption isotherm and (b) the corresponding pore size distribution of the yellow ZnO-500.

Raman scattering spectra were used to reveal the defects in the yellow ZnO mesocrystals. Figure 4 shows the room temperature Raman spectra of ZnO samples in the range of 200-800 cm^{-1}. The Raman peaks at 438 and 383 cm^{-1} are attributed to the typical Raman vibration modes of the wurtzite phase ZnO.[30,31] The peak at 331 cm^{-1} is also observed and assigned to the multiple phonon scattering process.[32] Besides these peaks, a small and suppressed peak at 585 cm^{-1} (Figure 4) has also been observed for ZnO-500, ZnO-800 and ZnO-ref samples, which results from the oxygen vacancies.[33,34] The peak intensity of the yellow ZnO-500 at 585 cm^{-1} is strongest among three samples, which implies that more oxygen vacancies exist in the yellow ZnO-500 mesocrystals.

Paper
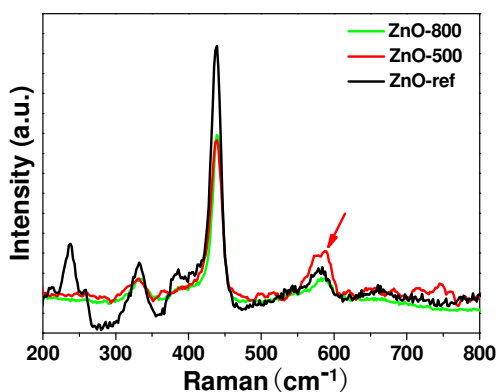
Fig. 4 Room-temperature Raman spectra of ZnO-ref and ZnO obtained from annealing Zn(OH)F precursors at different temperatures. Red arrow
300 points to the signal of oxygen vacancies.

X-ray photoelectron spectroscopy (XPS) was used to probe the chemical states of oxygen for providing deep insight into the oxygen vacancies in the ZnO mesocrystals, XPS spectra of O1s
305 are shown in Figure 5. The O1s spectra of the ZnO sample can be elucidated as the superposition of three peaks with Gaussian distribution, respectively appeared about 530.5, 531.9 and 533.4 eV. The peak at 533.4 eV was previously ascribed to the presence of loosely bound oxygen on the surfaces of ZnO.[35] The low
310 binding energy component appeared at ca. 530.5 eV comes from the O^{2-} ions in the wurtzite structure of a hexagonal Zn^{2+} ion array.[36] The medium binding energy peak, centered at about 531.9 eV, is attributed to O^{2-} in the oxygen deficient regions within the matrix of ZnO.[36,37] It is suggested that the intensity of
315 this peak is correlated with the variation in the concentrations of oxygen defects. Consequently, the change in the intensity of this peak could be partly ascribed to the variation in the concentrations of oxygen vacancies. From the O1s spectra, it is can be clearly seen that the peak at 531.9 eV is much stronger in
320 the ZnO-500 mesocrystals. The intensity of this peak decreases with increasing annealing temperature. As shown in Table S1 (Supporting Information), the area ratio of the peak at 531.9 eV to the peak at 530.5 eV is ca 0.68 and 0.58, and the area ratio of the peak at 533.4 eV to the peak at 531.9 eV is ca 0.022 and
325 0.011 for ZnO-500 and ZnO-800 samples, respectively. These results show that the oxygen vacancies and surface adsorptive oxygen in ZnO nanostructures decrease with an increase of annealing temperature, and more oxygen vacancies and surface adsorptive oxygen exist in the ZnO-500, which is consistent with
330 the Raman spectra results. In general, F ion can be doped into ZnO in the synthesis or annealing process. Comparing XPS spectra of ZnO-500 and ZnO-800 (Figure S1), it is found that F signal peak appears in ZnO-500, but doesn't appear in the ZnO-800. As well known, fluorine is the most electronegative element
335 and Zn-F binding energy is larger than that of Zn-O. When Zn(OH)F precursor is calcined at high temperature, some F atoms replace oxygen atoms and enter the crystal lattice. So, rich oxygen vacancies could be generated in ZnO-500 sample. Moreover, F is replaced gradually by O upon increasing the
340 calcination temperatures, and then the concentration of oxygen defects such as ZnO-800 decreased.
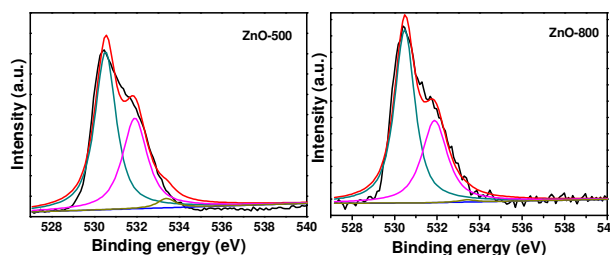
Fig. 5 XPS spectra for O1s of the ZnO-500 and ZnO-800 samples obtained by calcination of Zn(OH)F.

345 To investigate the influence of oxygen vacancies on the energy gap of ZnO samples prepared under different calcination temperatures, the optical properties of obtained ZnO mesocrystals were measured using UV-visible diffuse reflectance spectroscopy
350 (DRS). From Figure 6a, it can be found that ZnO-500 sample obtained by annealing Zn(OH)F precursor display a red shift to longer wavelength over than 400 nm by comparison with the ZnO-ref. The UV-visible diffuse reflectance spectra of ZnO samples obtained at different annealing temperatures are shown
355 in Figure S2. It can be found that ZnO samples exhibit a blue shift to shorter wavelength with annealing temperature increase (500→800 ℃). This wavelength shift is caused by the oxygen vacancies in ZnO-500 and ZnO-800 samples, already demonstrated by the Raman and XPS data analysis. The higher
360 concentration of oxygen defects is, the more wavelength red-shift is. It is thus confirmed that the oxygen vacancies can effectively expand yellow ZnO mesocrystals to the visible light absorption. For ZnO samples, the extrapolated value (a straight line to the x-axis) of Ephoton at α=0 represents absorption edge energy
365 corresponding to Eg that is the band gap of the sample, which follows plots of $(\alpha Ephoton)^2$ vs. the energy of absorbed light, here α and Ephoton gives the absorption coefficient and the discrete photon energy, respectively. Figure 6b shows the band-gap value of 3.17, 3.09 and 3.17 eV for ZnO-ref, ZnO-500 and
370 ZnO-800, respectively. The obtained ZnO-500 mesocrystal displays yellow color, in accordance with its narrow band. The band gap narrowing is much associated with the oxygen defect concentrations. According to the XPS and Raman results, ZnO-500 sample with the higher oxygen vacancy concentrations has
375 the narrower band-gap and could have the better visible light response than ZnO-800 and ZnO-ref samples, as discussed later.
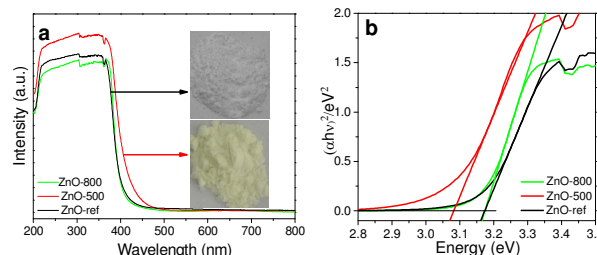
Fig. 6 (a) Diffuse reflectance spectra and (b) the plots of $(\alpha h\nu)^2$ vs. (hν) of ZnO samples, the inset shows the pictures of ZnO-500 and ZnO-ref
380 samples.

Electron paramagnetic resonance (EPR) spectra were measured for the as-made ZnO samples to further examine the intrinsic defect centers generated during the annealing Zn(OH)F
385 precursors. From the X-band EPR signals of the ZnO (Figure 7), it is found that they exhibit a similar type of paramagnetic defect centre, and showing a single EPR line at g = 1.95. On the other hand, the origins of these intrinsic defects have not been clearly unravelled. Rather, they were assigned controversially to shallow
390 donors, singly ionized oxygen defects, Zn vacancies, oxygen and

Zn interstitials.[38–41] The EPR signal at g = 1.99 is ascribed to surface defects. Because its g-value is close to that of a free electron, O_2^- superoxide ions generated from the oxygen or from -OH groups on ZnO surfaces were proposed,[42] which are in
395 agreement with IR data (Figure S3). However, this is currently under debate about the origin of the defect centre. According to previous literature reports,[43, 44] the EPR data could be simply elucidated as a core–shell model, here the signal at g = 1.95 is due to the 'bulk' (core) contribution and the one at g = 1.99
400 originates from the surface (shell) of the ZnO. According to the analysis of XPS, a large amount of deficient oxygen atoms exist in ZnO-500. So the defects in our ZnO samples can be simply attributed to oxygen vacancies and surface defects, and thus generating strong visible light photoluminescence (PL) emission,
405 as shown in Figure 8.
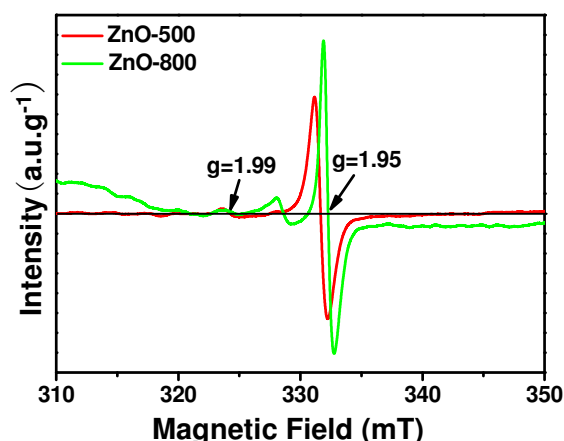
Fig. 7 X-Band EPR spectra of ZnO mesocrystals and ZnO-ref recorded at 140 K.

410   Figure 8 shows room temperature photoluminescent (PL) spectra of ZnO samples. A broad strong defect emission band from 370 nm to 800 nm centred at about 544 nm (green) of ZnO-800 is observed, which is different from the emission centred at 613 nm (red) of the yellow ZnO-500. Some models have been
415 proposed to unravel the origin of the defective emission in ZnO. Interstitial zinc and oxygen,[45] electronic transition from an interstitial Zn to a Zn vacancy,[46] and extrinsic impurities,[47] and the singly ionized oxygen vacancy[41,48,49] were hypothetically explained for the green PL in ZnO. For our ZnO samples, the
420 EPR spectrum with a g factor of 1.99 displays broadening and asymmetric characteristics, indicating that different types of oxygen-related defects might exist in the ZnO samples, and there also exists O^- anion adsorption on the ZnO surfaces.[50,51] Therefore, the singly ionized oxygen defects are most possibility
425 for the green PL emission of the ZnO-800. The PL peak at ca 613 nm in yellow ZnO-500 is suggested to be correlated with the intrinsic and excess oxygen due to chemisorptions, in accordance with the XPS analysis.
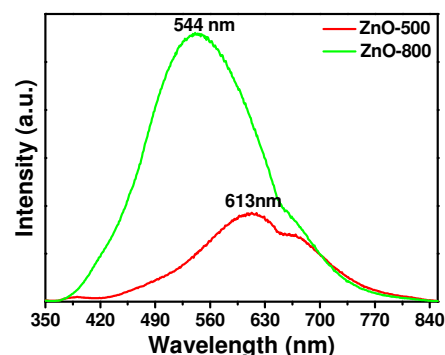
430 **Fig. 8** Room temperature solid-state PL spectra of ZnO samples (λ_{ex}= 325 nm)

   Based on the above results and the effect of the oxygen vacancies on the electronic structures of ZnO[23,24] and the oxygen
435 vacancies (Vö) defect energy levels calculated by Zheng et al.,[18] Figure 9 displays the effect of oxygen vacancy concentration on the energy level diagram for as-made ZnO from Zn(OH)F precursor. The oxygen vacancy level is < 0.9 eV below the conductive band-edge, it has no obvious effect on the band gap of
440 ZnO when the concentration of oxygen defects is low (Figure 9a). While abundant oxygen vacancies exist in ZnO, the oxygen vacancy level becomes delocalized and then overlapped with the conduction band edge, resulting in band gap narrowing (Figure 9b), which induces ZnO more efficient harvest of the visible
445 light. Taken together, the red shift of the absorption edge displayed in Figure 6 can be easily understood.
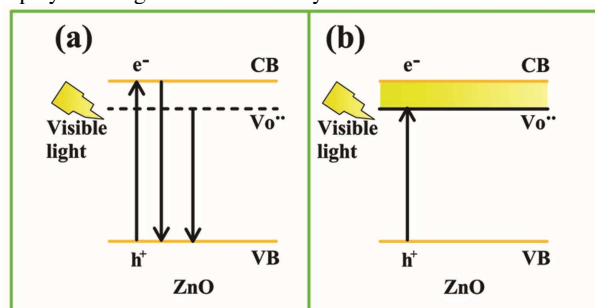
Fig. 9 The influence of oxygen vacancy concentrations on the band structures of as-prepared ZnO from Zn(OH)F precursor. (a) low and (b)
450 high concentration of oxygen vacancies.

   We performed the photocurrent response measurements on a photoelectrochemical test device prepared by drop casting ZnO-500, ZnO-800 and ZnO-ref dispersed alcohol solution onto a Ti
455 foil. The photoresponse of yellow ZnO-500 mesocrystal under visible light illumination is presented in Figure 10. It shows that the photocurrent increased stepwise in the on-off cycles, owing to the continuous increase of the charge carrier concentration with visible light illumination until saturation. This phenomenon can
460 be explained by the "light soaking" effect, previously observed in the photoanodes made from wide band-gap metal oxides such as SnO_2, TiO_2, etc.[52–54] This "light soaking" effect of visible light can be observed not only in charge generation but also in the charge decay after light switch-off. In addition, the photocurrent
465 response of ZnO-800 and ZnO-ref samples display a relatively low efficiency of photon-to-photocurrent conversion with several on/off illumination cycles. The photocurrent conversion efficiency of ZnO-500 mesocrystals is ca. 4 times higher than that of ZnO-800. The improvement of the photocurrents found for
470 yellow ZnO-500 has further demonstrated the ZnO-500 band gap decreasing, because abundant oxygen vacancies play a key role in

Paper www.rsc.org/[JOURNAL] | **[JOURNAL NAME HERE]**

narrowing the band gap instead of the formation the active centers or trap centers. Higher photocurrent indicates lower recombination of photogenerated e/h pairs, efficient charge
475 carrier transport, and more visible light absorption for ZnO-500 electrode, all these finally contribute to the improved visible photocatalytic activity. It is well known that semiconductor photocatalysis occurs through a series of oxidation and reduction reactions which take place on the light excited surfaces of
480 photocatalyst. In general, higher photocurrent means enhanced photocatalytic activity. These results have clearly shown the potential advantages of yellow ZnO-500 mesocrystals for highly improving photocatalytic activity.
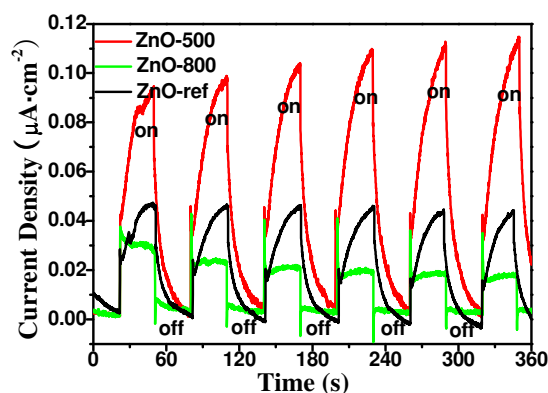
485 **Fig. 10** Current response vs time for the ZnO samples under chopped irradiation at a bias potential of 0.2 V vs Ag/AgCl ($\lambda \geq 400$ nm).

The photocatalytic activity of as-made ZnO sample was conducted by photodegradation of methyl blue (MB) dye under
490 visible-light irradiation, together with ZnO-ref for a comparison. Before light irradiation, the suspension was stirred in the dark to reach the sorption equilibrium of MB molecules on the photocatalyst, no obvious color change was found owing to little adsorption of MB over the catalyst. The contents of MB
495 molecules were measured from the maximum absorption peak at $\lambda = 664$ nm using UV-Vis absorption spectra. C/C_0 was utilized to represent the degradation efficiency, where C and C_0 is MB concentration at time t and 0, respectively. As shown in the Figure 11a, yellow ZnO-500 mesocrystals display the highest
500 visible light photocatalytic activity among three samples and about 85 % of MB dye molecules were decomposed within 3 h. The characteristic absorption peak of MB at 664 nm disappears gradually under visible light illumination (Figure 11b). ZnO-500 sample exhibits high visible light photo-degradation rate owing to
505 the narrow band-gap arising from rich oxygen vacancies.
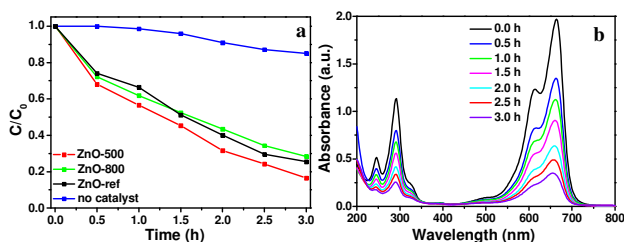
Fig. 11 (a) Comparison of photodecomposition of MB with different photocatalysts under visible light irradiation. (b) UV-Vis spectra of MB in
510 aqueous ZnO-500 dispersions as a function of irradiation time with visible light ($\lambda \geq 400$ nm).

In order to verify the stability and reusability of yellow ZnO-500 photocatalyst, we did recycling experiments by assessing the degradation of MB under the same conditions during the cycling

515 experiments. As displayed in Figure 12, yellow ZnO-500 for the degradation of MB exhibits a high activity and good stability after five cycling tests, about 78% of the original MB was decomposed, while it was 85 % for the first run, revealing that yellow ZnO-500 is stable enough under repeated photocatalytic
520 reaction. From the XRD pattern and SEM image (Figure S4) of yellow ZnO-500 after being reused for five times, it is found that yellow ZnO-500 morphology and structure did not change, which also confirms the stability of yellow ZnO-500 mesocrystal during recycling the photocatalytic process.
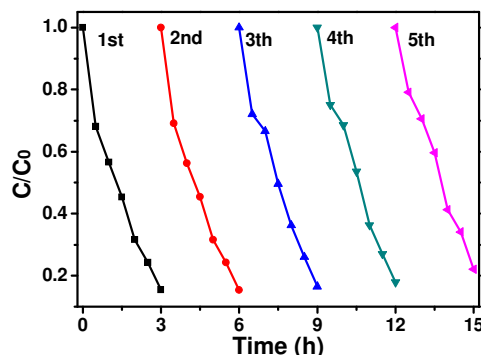
525 **Fig. 12** Cycling runs in the photodegradation of MB in the presence of yellow ZnO-500 mesocrystal under visible light irradiation.

Conclusions

530 In summary, we have synthesized a novel yellow colored ZnO-500 mesocrystals by fabricating Zn(OH)F precursors. The high concentration of oxygen vacancies in yellow ZnO-500 mesocrystals builds an impurity level near the conduction band
535 and induces the band gap narrowing, which results in yellow colored ZnO. It is found that highly ordered porous ZnO-500 mesocrystals are favourable for directional transport and high efficient separation of charge carriers. The photocurrent response tests under visible light illumination demonstrated the enhanced
540 visible light absorption capability of yellow ZnO-500 mesocrystals, which exhibits good photocatalytic activity and stability in photo decomposition of MB. More importantly, yellow ZnO-500 mesocrystal is very stable for at least one year in air. Our present strategy has some advantages, such as simple,
545 convenient, controllable, and reproducible. It is believed that this work may also be applicable to fabricate other nanostructures based on defect engineering and provide potential applications of tailored solar energy conversion devices with a low cost.

555 ## Notes and references

‡ Additional figures are given in supporting information.

1 H. Tong, S. X. Ouyang, Y. P. Bi, N. Umezawa, M. Oshikiri and J. H. Ye, *Adv. Mater.,* 2012, **24**, 229−251.
560 2 H. Cölfen and S. Mann, *Angew. Chem., Int. Ed.,* 2003, **42**, 2350−2365.
3 M. Niederberger and H. Cölfen, *Phys. Chem. Chem. Phys.,* 2006, **8**, 3271−3287.

Paper

4 X. F. Yang, J. L. Qin, Y. Li, R. X. Zhang and H. Tang, *J. Hazardous Mater.,* 2013, **261**, 342–350.

5 F. Ye, Y. Peng, G. Y. Chen, B. Deng and A. W. Xu, *J. Phys. Chem. C,* 2009, **113**, 10407–10415.

6 Z. F. Bian, T. Tachikawa, P. Zhang, M. Fujitsuka and T. Majima, *J. Am. Chem. Soc.,* 2014, **136**, 458–465.

7 N. Daneshvar, D. Salari and A. R. Khataee, *J. Photochem. Photobiol. A,* 2004, **162**, 317□322.

8 Q. Zhu, Y. Peng, L. Lin, C. M. Fan, G. Q. Gao, R. X. Wang and A. W. Xu, *J. Mater. Chem. A,* 2014, **2**, 4429–□4437.

9 C. M. Fan, Y. Peng, Q. Zhu, L. Lin, R. X. Wang and A. W. Xu, *J. Phys. Chem. C,* 2013, **117**, 24157–24166.

10 Z. K. Zheng, B. B. Huang, X. D. Meng, J. P. Wang, S. Y. Wang, Z. Z. Lou, Z. Y. Wang, X. Y. Qin, X. Y. Zhang and Y. Dai, *Chem. Commun.,* 2013, **49**, 868–870.

11 I. Justicia, P. Ordejon, G. Canto, J. L. Mozos, J. Fraxedes, G. A. Battiston, R. Gerbasi and A. Figueras, *Adv. Mater.,* 2002, **14**, 1399–1402.

12 F. Zuo, L. Wang, T. Wu, Z. Y. Zhang, D. Borchardt and P. Y. Feng, *J. Am. Chem. Soc.,* 2010, **132**, 11856–11857.

13 I. Justicia, G. Garcia, L. Vázquez, J. Santiso, P. Ordejón, G. Battiston, R. Gerbasi and A. Figueras, *Sens. Actuator B*, 2005, **109**, 52–56.

14 A. F. Holleman and E. Wiberg, Academic Press: San Diego, CA, 2001, p 499.

15 N. R. Aghamalyan, I. A. Gambaryan, E. Kh. Goulanian, R. K. Hovsepyan, R. B. Kostanyan, S. I. Petrosyan, E. S. Vardanyan and A. F. Zerrouk, *Semicond. Sci. Technol.*, 2003, **18**, 525–529.

16 J. D. Ye, S. L. Gu, S. M. Zhu, F. S. Qin, M. Liu, W. Liu, X. Zhou, L. Q. Hu, R. Zhang, Y. Shi and Y. D. Zheng, *J. Appl. Phys.,* 2004, 96, 5308–5310.

17 Y. Huo and Y. H. Hu, *Ind. Eng. Chem. Res.,* 2012, **51**, 1083–1085.

18 Y. H. Zheng, C. Q. Chen, Y. Y. Zhan, X. Y. Lin, Q. Zheng, K. M. Wei, J. F. Zhu and Y. J. Zhu, *Inorg. Chem.,* 2007, **46**, 6675–6682.

19 A. B. Patil, K. R. Patil and S. K. Pardeshi, *J. Solid State Chem.,* 2011, 184, 3273–3279.

20 J. C. Wang, P. Liu, X. Z. Fu, Z. H. Li, W. Han and X. X. Wang, *Langmuir,* 2009, **25**, 1218–1223.

21 M. Y. Guo, A. M. C. Ng, F. Z. Liu, A. B. Djurisic, W. K. Chan, H. M. Su and K. S. Wong, *J. Phys. Chem. C,* 2011, **115**, 11095–11101.

22 X. J. Bai, L. Wang, R. L. Zong, Y. H. Lv, Y. Q. Sun and Y. F. Zhu, *Langmuir,* 2013, **29**, 3097–3105.

23 J. P. Wang, Z. Y. Wang, B. B. Huang, Y. D. Ma, Y. Y. Liu, X. Y. Qin, X. Y. Zhang, Y. Dai, *ACS Appl. Mater. Interf.,* 2012, **4**, 4024–4030.

24 S. A. Ansari, M. M. Khan, S. Kalathil, A. Nisar, J. Leea, M. H. Cho, *Nanoscale* 2013, **5**, 9238–9246.

25 Y. H. Lv, C. S. Pan, X. G. Ma, R. L. Zong, X. J. Bai, Y. F. Zhu, *Appl. Catal. B: Envi.*, 2013, **138–139**, 26–32.

26 Y. H. Lv, W. Q. Yao, X. G. Ma, C. S. Pan, R. L. Zong and Y. F. Zhu, *Catal. Sci. Technol.,* 2013, **3**, 3136–3146.

27 N. Uekawa, J. Kajiwara, N. Mochizuki, K. Kakegawa and Y. Sasaki, *Chem. Lett.,* 2001, **30**, 606–607.

28 N. Uekawa, M. Mochizuki, J. Kajiwara, F. Mori, Y. J. Wu and K. Kakegawa, *Phys. Chem. Chem. Phys.*, 2003, **5**, 929–934.

29 B. Chavillon, L. Cario, A. Renaud, F. Tessier, F. Chevire, M. Boujtita, Y. Pellegrin, E. Blart, A. Smeigh, L. Hammarstrom, F. Odobel and S. Jobic, *J. Am. Chem. Soc.,* 2012, **134**, 464–470.

30 R. Y. Sato-Berru, A. Vázquez-Olmos, A. L. Fernández-Osorio and S. Sotres-Martínez, *J. Raman Spectrosc.,* 2007, **38**, 1073–1076.

31 Ü. Özgür, Y. I. Alivov, C. Liu, A. Teke, M. A. Reshchikov, S. Dogan, V. Avrutin, S. J. Cho and H. Morkoc, *J. Appl. Phys.,* 2005, **98**, 41301–41404.

32 R. P. Wang, G. Xu and P. Jin, *Phys. Rev. B,* 2004, **69**, 113303–113306.

33 G. J. Exarhos and S. K. Sharma, *Thin Solid Films,* 1995, **270**, 27–32.

34 M. Rajalakshmi, A. K. Arora, B. S. Bendre and S. Mahamuni, *J. Appl. Phys.,* 2000, 87, 2445–2448.

35 J. C. C. Fan and J. B. Goodenough, *J. Appl. Phys.,* 1977, 48, 3524–3531.

36 S. Park, T. Ikegami, K. Ebihara, *Thin Solid Films,* 2006, **513**, 90–94.

37 M. Chen, X. Wang, Y. H. Yu, Z. L. Pei, X. D. Bai, C. Sun, R. F. Huang and L. S. Wen, *Appl. Surf. Sci*., 2000, **158**, 134–140.

38 B. Yu, C. Zhu, F. Gan and Y. Huang, *Mater. Lett.,* 1998, **33**, 247–250.

39 S. M. Evans, N. C. Giles, L. E. Halliburton and L. A. Kappers, *J. Appl. Phys.,* 2008, **103**, 43710–43716.

40 N. Y. Garces, L. Wang, L. Bai, N. C. Giles, L. E. Halliburton and G. Cantwell, *Appl. Phys. Lett.,* 2002, **81**, 622–624.

41 K. Vanheusden, W. L. Warren, C. H. Seager, D. R. Tallant, J. A. Voigt and B. E. Gnade, *J. Appl. Phys.,* 1996, **79**, 7983–7990.

42 V. Ischenko, S. Polarz, D. Grote, V. Stavarache, K. Fink, M. Driess, *Adv. Funct. Mater.,* 2005, **15**, 1945–1954.

43 J. J. Schneider, R. C. Hoffmann, J. Engstler, S. Dilfer, A. Klyszcz, E. Erdem, P. Jakes and R. A. Eichel, *J. Mater. Chem.,* 2009, **19**, 1449–1457.

44 J. J. Schneider, R. C. Hoffmann, J. Engstler, A. Klyszcz, E. Erdem, P. Jakes, R. A. Eichel, L. Pitta-Bauermann and J. Bill, *Chem. Mater.,* 2010, **22**, 2203–2212.

45 M. Liu, A. H. Kitai and P. Mascher, *J. Lumin.,* 1992, **54**, 35–42.

46 E. G. Bylnder, *J. Appl. Phys.,* 1978, **49**, 1188–1192.

47 R. Dingle, *Phys. Rev. Lett.,* 1969, **23**, 579–581.

48 C. M. Mo, Y. H. Li, Y. S. Liu, Y. Zhang and L. D. Zhang, *J. Appl. Phys.,* 1998, **83**, 4389–4391.

49 M. J. Zheng, L. D. Zhang, G. H. Li and W. Z. Shen, *Chem. Phys. Lett.*, 2002, 363, 123–128.

50 M. Anpo and Y. Kubokawa, *J. Phys. Chem.*, 1984, **88**, 5556–5660.

51 G. J. Guan, L. Yang, Q. S. Mei, K. Zhang, Z. P. Zhang and M. Y. Han, *Anal. Chem.,* 2012, **84**, 9492–9497.

52 P. Tiwana, P. Docampo, M. B. Johnston, L. M. Herz and H. J. Snaith, *Energy Environ. Sci.*, 2012, **5**, 9566–9573.

53 Q. Wang, Z. Zhang, S. M. Zakeeruddin and M. Gratzel, *J. Phys. Chem. C,* 2008, **112**, 7084–7092.

54 A. Listorti, C. Creager, P. Sommeling, J. Kroon, E. Palomares, A. Fornelli, B. Breen, P. R. F. Barnes, J. R. Durrant, C. Law and B. ÓRegan, *Energy Environ. Sci.,* 2011, **4**, 3494–3501.

Graphic Abstract:
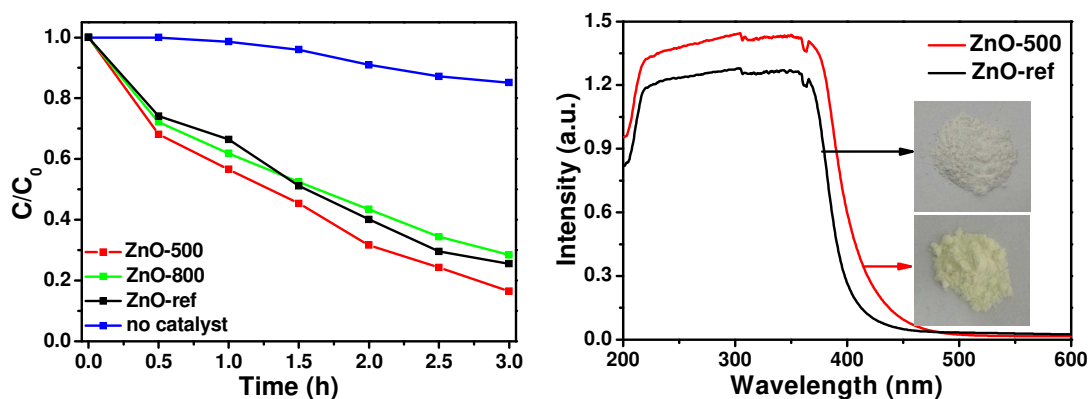
In this work, we present a novel and facile approach to prepare yellow ZnO mesocrystals from Zn(OH)F precursor. The as-prepared yellow ZnO show narrow band-gap (Eg = 3.09 eV) and visible light photocatalytic activity, which is due to the existence of abundant oxygen vacancies and vectorially aligned nanoparticles.